

# **Slip Continuity in Explicit Crystal Plasticity Simulations Using Nonlocal Continuum and Semi-discrete Approaches**

**by Richard Becker**

**ARL-MR-0838**

**January 2013**

## **NOTICES**

### **Disclaimers**

The findings in this report are not to be construed as an official Department of the Army position unless so designated by other authorized documents.

Citation of manufacturer's or trade names does not constitute an official endorsement or approval of the use thereof.

Destroy this report when it is no longer needed. Do not return it to the originator.

# **Army Research Laboratory**

Aberdeen Proving Ground, MD 21005

---

**ARL-MR-0838****January 2013**

---

## **Slip Continuity in Explicit Crystal Plasticity Simulations Using Nonlocal Continuum and Semi-discrete Approaches**

**Richard Becker**

**Weapons and Materials Research Directorate, ARL**

REPORT DOCUMENTATION PAGE			Form Approved OMB No. 0704-0188		
<p>Public reporting burden for this collection of information is estimated to average 1 hour per response, including the time for reviewing instructions, searching existing data sources, gathering and maintaining the data needed, and completing and reviewing the collection information. Send comments regarding this burden estimate or any other aspect of this collection of information, including suggestions for reducing the burden, to Department of Defense, Washington Headquarters Services, Directorate for Information Operations and Reports (0704-0188), 1215 Jefferson Davis Highway, Suite 1204, Arlington, VA 22202-4302. Respondents should be aware that notwithstanding any other provision of law, no person shall be subject to any penalty for failing to comply with a collection of information if it does not display a currently valid OMB control number.</p> <p><b>PLEASE DO NOT RETURN YOUR FORM TO THE ABOVE ADDRESS.</b></p>					
1. REPORT DATE (DD-MM-YYYY) January 2013		2. REPORT TYPE DRI		3. DATES COVERED (From - To) October 2010 to September 2012	
4. TITLE AND SUBTITLE Slip Continuity in Explicit Crystal Plasticity Simulations Using Nonlocal Continuum and Semi-discrete Approaches			5a. CONTRACT NUMBER		
			5b. GRANT NUMBER		
			5c. PROGRAM ELEMENT NUMBER		
6. AUTHOR(S) Richard Becker			5d. PROJECT NUMBER FY11-WMR-017		
			5e. TASK NUMBER		
			5f. WORK UNIT NUMBER		
7. PERFORMING ORGANIZATION NAME(S) AND ADDRESS(ES) U.S. Army Research Laboratory ATTN: RDRL-WMP-C Aberdeen Proving Ground, MD 21005			8. PERFORMING ORGANIZATION REPORT NUMBER  ARL-MR-0838		
9. SPONSORING/MONITORING AGENCY NAME(S) AND ADDRESS(ES)			10. SPONSOR/MONITOR'S ACRONYM(S)		
			11. SPONSOR/MONITOR'S REPORT NUMBER(S)		
12. DISTRIBUTION/AVAILABILITY STATEMENT Approved for public release; distribution unlimited.					
13. SUPPLEMENTARY NOTES					
14. ABSTRACT <p>Slip continuity across element boundaries in explicit finite element simulations is enforced through nonlocal penalty constraints applied to continuum crystal plasticity relations and in a nonlocal, semi-discrete crystal slip model. The continuity constraints provide additional coupling within the plastic deformation field, and a length scale effect is introduced. The deformation field becomes more diffuse with reduced physical size of the model region and the strength increases. Consideration of the physical spacing of dislocations and the typical size of dislocation cells in deformed metals elicits concerns about the applicability of continuum slip models with sub-micron spatial resolution.</p>					
15. SUBJECT TERMS <p>Crystal plasticity, nonlocal, gradient, dislocation, Director's Research Initiative (DRI)</p>					
16. SECURITY CLASSIFICATION OF:			17. LIMITATION OF ABSTRACT  UU	18. NUMBER OF PAGES  30	19a. NAME OF RESPONSIBLE PERSON Richard Becker
a. REPORT Unclassified	b. ABSTRACT Unclassified	c. THIS PAGE Unclassified			19b. TELEPHONE NUMBER (Include area code) (410) 278-7980

---

## Contents

---

<b>List of Figures</b>	<b>iv</b>
<b>List of Tables</b>	<b>iv</b>
<b>Acknowledgment</b>	<b>v</b>
<b>1. Objective</b>	<b>1</b>
<b>2. Approach</b>	<b>1</b>
2.1 Flux Constraint .....	1
2.2 Model Geometry .....	3
<b>3. Results</b>	<b>3</b>
3.1 Single Crystal Simulations .....	3
3.2 Polycrystal Simulations .....	10
<b>4. Physical Size Scale Considerations</b>	<b>14</b>
4.1 Semi-discrete Dislocation Model .....	15
<b>5. Conclusions</b>	<b>17</b>
<b>6. References</b>	<b>19</b>
<b>7. Transitions</b>	<b>21</b>
<b>Distribution List</b>	<b>22</b>

---

## List of Figures

---

Figure 1. Initial configuration for the single crystal and the crystal lattice orientation. The bottom is fixed and the top is moved to the right. Periodic boundary conditions are applied coupling the left and right hand sides. ....	4
Figure 2. Distribution of the nonlocal contribution to the strength on the slip system aligned vertically in the crystal, for the crystal thicknesses indicated, at shear strains of 0.03 and 0.05.....	5
Figure 3. Distribution of the normalized slip rate for single crystals of the indicated thickness and at shear strains of 0.03 and 0.05. The slip rates are normalized by the applied shear rate.....	7
Figure 4. Shear stress-shear strain response predicted for the four crystal thicknesses. ....	8
Figure 5. Comparison of nonlocal stress and the slip rate for the $20 \times 100$ and $40 \times 200$ element simulations of the 5- $\mu\text{m}$ -thick single crystal. The results are shown at a 0.05 shear strain. ....	9
Figure 6. Grain structure (a) and finite element mesh and (b) for the polycrystal simulations. ....	10
Figure 7. Normalized slip rate distribution for simple shear deformation of idealized polycrystals with heights of 330, 33, and 3.0 $\mu\text{m}$ . The color scale is the same for all three plots.....	11
Figure 8. Nonlocal strength contributions on the three slip systems for polycrystal model sizes of 330, 33, and 3.3 $\mu\text{m}$ . The color scales are consistent within each row.....	12
Figure 9. Shear stress strain response for three different size scales of idealized polycrystals. ....	13
Figure 10. Change in crystal lattice orientation, in degrees, at 0.025 shear strain for the 330- and 3.3- $\mu\text{m}$ -high polycrystals. ....	14
Figure 11. Number of dislocations passing through each element for the discrete dislocation simulations. The center 80 $\mu\text{m}$ is omitted from the 100- $\mu\text{m}$ crystal to highlight the gradients at the top and bottom surfaces.....	16
Figure 12. Number of dislocations currently within each element for the discrete dislocation simulations. The center 80 $\mu\text{m}$ is omitted from the 100- $\mu\text{m}$ crystal to highlight the gradients at the top and bottom surfaces.....	16

---

## List of Tables

---

Table 1. Average number of dislocations per element expected in the simulations of for well-annealed, lightly deformed and heavily deformed metals. ....	14
--	----

---

## **Acknowledgment**

---

I am grateful for the support of this work through the Director's Research Initiative at the U.S. Army Research Laboratory, FY11-WMR-017.

INTENTIONALLY LEFT BLANK.



---

## 1. Objective

---

The objectives of this work are to incorporate dislocation transport into a continuum crystal plasticity formulation, implement the model into a finite element code, and evaluate the model's ability to capture effects of dislocation aggregation, specifically, the grain boundary strengthening effects and stress concentrations at grain boundaries.

---

## 2. Approach

---

The intent is to develop an enhancement to traditional continuum crystal plasticity models that can be readily incorporated into existing finite element implementations and run with minimal additional computational overhead. This goal is facilitated by targeting explicit dynamic solutions where, because of the relatively small time steps, it is often possible to impose additional constraints through an operator-split approach. Details of the crystal plasticity model and the time integration are reported elsewhere (*1*), and only the modifications related to the constraint of the dislocation flux are presented herein.

### 2.1 Flux Constraint

The basic model is that dislocations move along the slip direction from one element to another. The flux of dislocations crossing an element boundary for each slip system is

$$\dot{\phi} = \rho_{dis}^{\alpha} v^{\alpha} \mathbf{s}^{\alpha} \cdot \mathbf{n}_f, \quad (1)$$

where  $\rho_{dis}^{\alpha}$  is the dislocation density,  $v^{\alpha}$  is the dislocation velocity,  $\mathbf{s}^{\alpha}$  is the slip direction, and  $\mathbf{n}_f$  is the outward normal to the given element face. Continuity is enforced by requiring that the dislocation flux exiting through an element face equals the flux entering the adjacent element through the common face. The dot product in equation 1 accounts for the orientation of the slip system with respect to the element face. It is zero if the slip direction is parallel to the face. This provides the opportunity for sharp jumps in slip rates across parallel slip planes while enforcing continuity along slip planes.

The dislocation density, velocity and the Burgers vector,  $b$ , are related to the continuum slip rate by Orowan's equation

$$\dot{\gamma}^{\alpha} = \rho_{dis}^{\alpha} v^{\alpha} b. \quad (2)$$

For a shared element face, and assuming that the Burgers vector is constant and that the slip directions are closely aligned across the interface, the continuity error in the accumulated dislocation flux between elements can be approximated as

$$[(\gamma^\alpha)_{neighbor} - (\gamma^\alpha)_e] \mathbf{s}^\alpha \cdot \mathbf{n}_f = E_f^\alpha. \quad (3)$$

The subscripts  $e$  and  $neighbor$  on the accumulate slip,  $\gamma^\alpha$ , denote, respectively, the element of interest and the neighbor sharing the face. The approach taken is to penalize the error. It is not necessary to assume that the Burgers vectors are equal or that the slip directions in the adjacent elements are aligned, but these simplifications are made for expedience and coding clarity in this initial implementation.

With some adjustments ( $I$ ), the driving force for the penalty method, equation 3 is summed as

$$\frac{1}{\Sigma |\mathbf{s}^\alpha \cdot \mathbf{n}_f|} \sum_{f=1}^{N_{faces}} \frac{1}{L_f} \text{Sign}(\gamma^\alpha) [(\gamma^\alpha)_{neighbor} - (\gamma^\alpha)_e] |\mathbf{s}^\alpha \cdot \mathbf{n}_f| = E^\alpha. \quad (4)$$

$L_f$  is the distance between element centroids associated with the particular element face. It is intended to provide a larger penalty if the slip difference occurs on a smaller spatial grid.  $E^\alpha$  in equation 4 is a weighted sum of unsigned slip gradients on a slip system for a given element. If the value is positive, slip is deficient in the element and additional slip is promoted. If the value is negative, further slip is impeded. It is significant that a constant gradient results in face contributions that sum to zero. Hence, a constant gradient is not suppressed. The excess dislocations associated with the gradient are assumed to be uniformly distributed.

Close examination of equation 4 reveals that the constraint resembles the micro force balance in several gradient formulations (2, 3). Hence, with a small coding change using the square of  $L_f$  in the denominator, the implementation approximates a simplified version of established gradient models.

The flow strength in the power law slip rate model,  $g^\alpha$ , is adjusted, based on the nonlocal contribution, to increase or reduce the resistance to continued deformation

$$g^\alpha = g_0^\alpha - \mu p_1 \tanh\left(b^2 \tilde{E}^\alpha \frac{p_2}{p_1}\right). \quad (5)$$

Here,  $p_1$  and  $p_2$  are dimensionless parameters,  $\mu$  is some average shear modulus for the crystal, and  $b$  is the Burgers vector. The base crystal strength,  $g_0^\alpha$ , could be a function of slip to capture strain hardening, but it is assumed constant in these analyses to simplify interpretation of the results. The hyperbolic tangent function is used to cap the influence of the nonlocal term. The contribution is approximately linear,  $\sim \mu p_2 b^2 \tilde{E}^\alpha$ , while the argument is small, and it is capped at a constant value of  $\pm \mu p_1$ . The penalty parameters are chosen as  $p_1 = 5 \times 10^{-4}$  and  $p_2 = 10000$ . In all of the nonlocal continuum simulations, the base flow strength is  $g_0^\alpha = 33.33$  MPa; the density is  $\rho_0 = 2.7$  g/cm<sup>3</sup>; the Burgers vector is  $b = 0.3$  nm; and shear modulus is  $\mu = 25,650$  MPa. A low power law rate exponent,  $m = 0.005$ , is chosen to provide nearly rate-independent behavior while still smoothing the transition from elastic to plastic response at the slip system flow strength,  $g^\alpha$ .

## 2.2 Model Geometry

An idealized two-dimensional crystal geometry is used for these analyses. The crystal consists of three slip systems set in an equilateral triangle configuration. This allows a multitude of slip modes. The model was implemented in the large-scale parallel, explicit finite element code ALE3D (4), and details are provided elsewhere (1). The crystal plasticity constitutive model existed previously (5) and the strengthening terms in equation 5 due to the nonlocal effects were a straightforward addition.

Constant strain quadrilateral elements with hourglass control (6) are used for all of the simulations. Elements in which all four faces are adjacent to an element of the same initial orientation are interior elements, and gradients are computed directly as indicated in equation 7. Elements with fewer than four faces contacting regions of the same orientation are either on grain boundaries or model boundaries. The face is flagged for these elements, and a parameter is checked to see whether it is treated as a zero flux boundary or a free boundary with no slip impedance. For the non-interior elements with zero-flux boundaries, ghost elements with opposite slip are assumed across the flagged faces. Grain boundaries and surfaces with applied boundary conditions are treated in this manner. For free surfaces and periodic boundaries, the ghost element across the flagged face is set with the same slip so that these interfaces do not contribute to the gradient.

---

## 3. Results

---

The effect of the slip continuity constraint (slip gradient) is evaluated on two configurations, each at multiple length scales. All simulations are two-dimensional. The first configuration is simple shear of a single crystal with one of the slip planes initially aligned orthogonal to the shear direction. This creates single slip conditions for a straightforward evaluation of the model. The second configuration is a polycrystal constructed from regular hexagons. The orientation of the crystal lattice for each grain is chosen at random.

### 3.1 Single Crystal Simulations

Single crystal calculations were run at four size scales using a  $20 \times 100$  mesh of square elements (figure 1). Velocity boundary conditions are applied to the upper and lower surfaces to shear the top of the crystal to the right. Initial velocities of all interior nodes are prescribed consistent with simple shear to eliminate ringing as the explicit dynamic calculation starts. Periodic boundary conditions are applied to the lateral surfaces to mimic an infinitely wide crystal. The heights of the single crystals simulated were 50, 5, 1, and 0.5  $\mu\text{m}$ , and the width of the simulation box was 20% of the height in each case. Although the width is irrelevant with the periodic boundary conditions, multiple elements are used across the width to demonstrate that the boundary

conditions are applied properly. Slip transmission is restrained on the upper and lower boundaries, and slip transmission is unimpeded on the lateral, periodic boundaries.

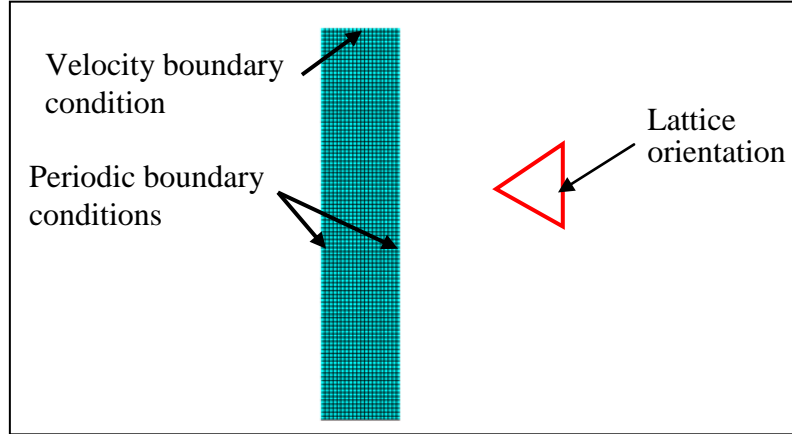


Figure 1. Initial configuration for the single crystal and the crystal lattice orientation. The bottom is fixed and the top is moved to the right. Periodic boundary conditions are applied coupling the left and right hand sides.

The nonlocal strength contribution to equation 5 is shown in figure 2 for the four crystal sizes and at two shear strains. The largest crystal is on the left and the smallest is on the right. The top row shows the distribution at a shear strain of 0.03 and the shear strain is 0.05 in the bottom row. The color scales are different for each crystal size, but the scales at each crystal size are the same at 0.03 and 0.05 shear strains to highlight the evolution.

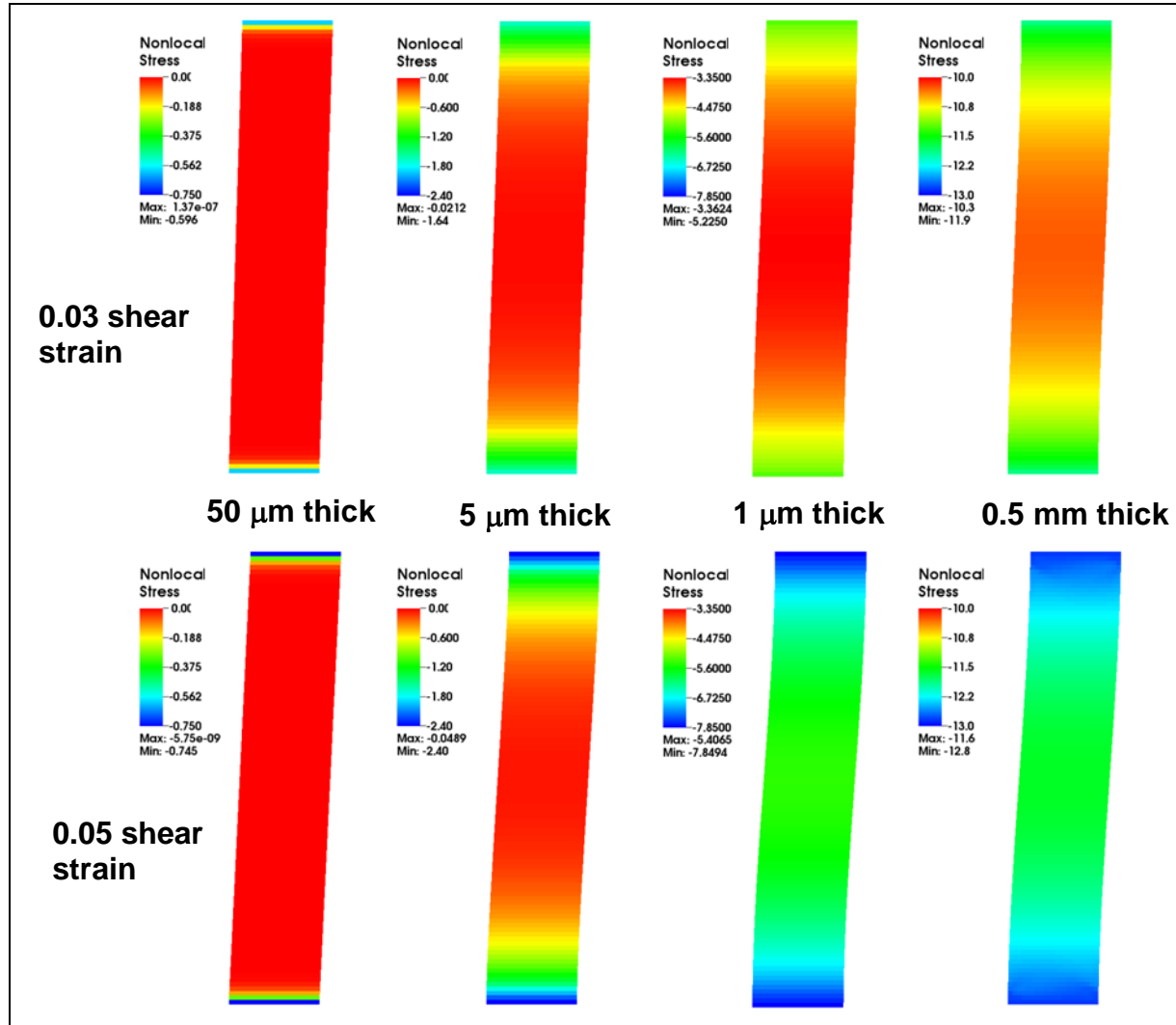


Figure 2. Distribution of the nonlocal contribution to the strength on the slip system aligned vertically in the crystal, for the crystal thicknesses indicated, at shear strains of 0.03 and 0.05.

The magnitude of the nonlocal strength contribution and the relative depth that the distribution penetrates from the surfaces increases as the crystal thickness is decreased. The sharpest gradients are expected at the crystal surfaces where the slip transmission is impeded. For the 50- $\mu\text{m}$  crystal the strength is increased only within a few elements of the surface, corresponding to a few microns. The central portion of the crystal sees no gradient or strengthening effect, even as the strain increases from 0.03 to 0.05. The boundary layer also appears to penetrate a few microns in the 5- $\mu\text{m}$ -thick crystal simulation. However, a smaller portion of the crystal is nearly free of gradient effects for this smaller crystal. At yet smaller crystal thicknesses, the gradient effect penetrates the full crystal thickness, and the evolution with increasing deformation is evident. The strength at the center is elevated significantly by a strain of 0.03, and it continues to increase with further deformation.

The minimum and maximum values are indicated in each of the plots. Except for the smallest crystal, the difference between the maximum and minimum increases as the crystal size decreases, and the difference also increases with increasing strain. The increase with strain indicates that the gradient is still evolving at a shear strain of 0.05. The trends are different for the 0.5- $\mu\text{m}$  crystal because the gradient strengthening is beginning to run up against the cap set by the hyperbolic tangent function in equation 5. With continued deformation, the gradient strengthening is becoming more uniform, albeit at a higher level.

The momentum balance in the vertical direction ( $y$ -direction) dictates that the  $y$ -gradient in the  $y$ -direction stress component is balanced by the horizontal ( $x$ -direction) gradient in the shear stress. Since the periodic boundary conditions require that all horizontal gradients are zero, the stress in the  $y$ -direction should be constant. The magnitude of the  $y$ -direction stress is not determined by the momentum equation, just that it is constant. The calculations show a constant  $y$ -direction stress to five significant digits.

More important for current purposes is the momentum balance in the horizontal direction. The lack of stress gradients in the horizontal direction requires the shear stress to be constant through the thickness. The simulations show that the shear stress is constant to five significant digits. While the  $x$ -direction stress must be constant in the  $x$ -direction, the symmetry conditions and momentum equations provide no further constraints restricting its gradient in the  $y$ -direction.

The normalized slip rates corresponding to the configurations in figure 2 are shown in figure 3. Again, the largest crystal is on the left and the smallest is on the right. The top row contains results at a shear strain of 0.03, and results at a shear strain of 0.05 are shown in the bottom row. The plots are normalized by the applied shear strain rate so that a value of 1.0 would indicate a uniform shear. Since the shear stress and the reference strength are both constant, the slip rate is approximately related to the gradient term in equation 5. Second-order factors influencing the slip rate include the change in lattice orientation and non-zero components of the  $x$ -direction and  $y$ -direction stresses that modify the resolved shear stress.

The slip rate follows the same trends as the nonlocal hardening contribution. The variation in slip rate is greater for the smaller crystals; and, except for the smallest crystal, the differences are greater with increased deformation. As a result of the boundary conditions, slip rates are low at top and bottom boundaries compared to the center regions. This results in the sigmoidal deformed shapes. More severe differences in slip rate result in greater deviation from a linear shear deformation profile. The slip rates for the 0.5- $\mu\text{m}$  crystal become more uniform at the higher deformation because the gradient term is capped by the hyperbolic tangent function. The strength is more uniform, which results in a more uniform slip rate.

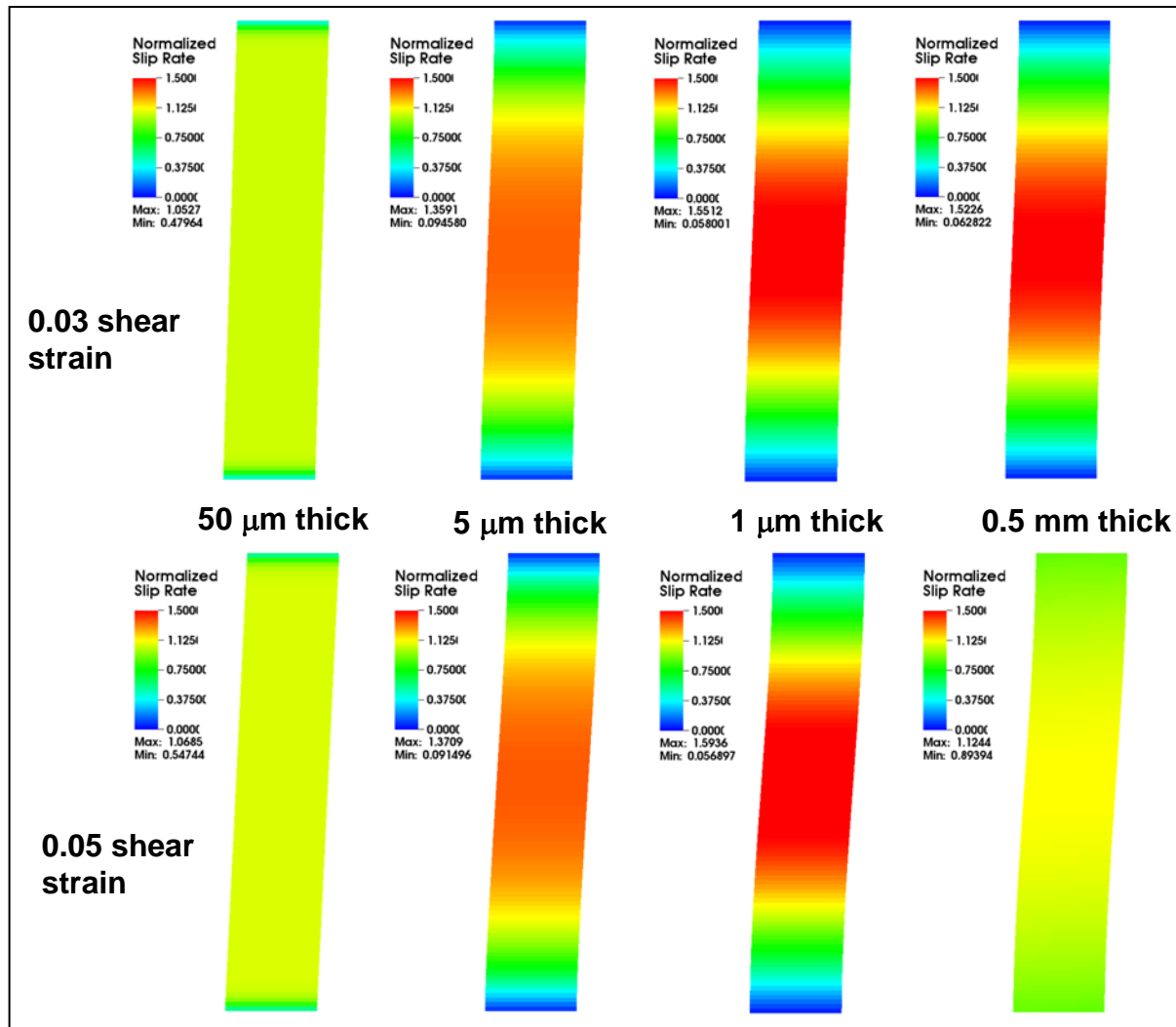


Figure 3. Distribution of the normalized slip rate for single crystals of the indicated thickness and at shear strains of 0.03 and 0.05. The slip rates are normalized by the applied shear rate.

The shear stress-shear strain responses for the various crystal thicknesses are plotted in figure 4. The curves are identical through the linear elastic regime, and all yield at approximately the same stress, approximately 34 MPa. The applied shear rate is 50 times the reference shear rate; and, accounting for the strain rate sensitivity, the apparent yield strength is calculated from the power law rate equation to be 33.99 MPa rather than the reference shear strength of 33.33 MPa.

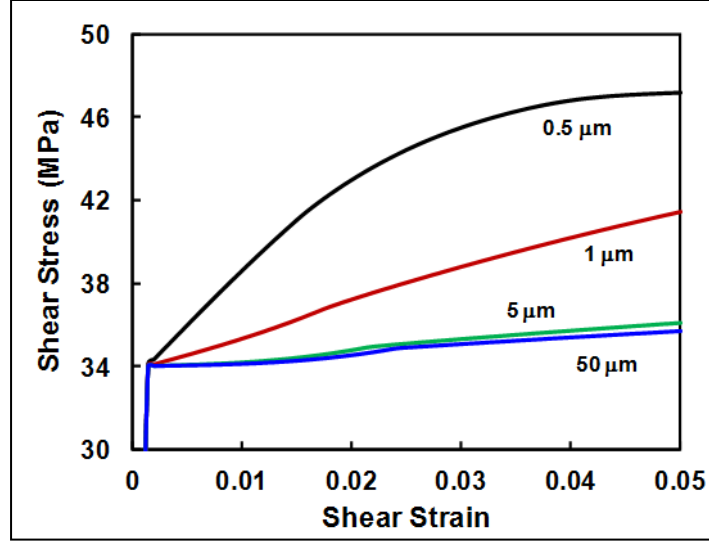


Figure 4. Shear stress-shear strain response predicted for the four crystal thicknesses.

The stress shows the expected trend of increasing strength at the smaller crystal sizes. This is directly related to the nonlocal strength in figure 2. The nonlinear dependence on specimen dimensions is due to dividing by the element size squared in the modification to equation 5. The strain hardening rate is fairly consistent with increasing strain for the three larger crystal sizes but not for the smallest. Stress in the 0.5- $\mu\text{m}$  crystal peaks as the hyperbolic tangent function places a cap on the nonlocal strength contribution. This is also consistent with the results presented in figures 2 and 3. A final observation from figure 4 is the kink that is most evident in the larger two specimens near a strain of 0.02. This marks the transition from single slip at lower strains to slip on two slip systems at larger strains. As the crystal lattice rotates and stresses build in the  $x$  and  $y$  directions, the crystals are able to accommodate the deformation more easily with multiple active systems. Due to the angle of the slip plane, slip constraints at the boundaries are not as severe for the second slip system, so the strain hardening rate is reduced.

The effect of mesh resolution on the solution is investigated by rerunning the 5- $\mu\text{m}$ -thick simulation using twice as many elements in each direction. The results from the  $40 \times 200$  mesh are shown along side of the  $20 \times 100$  mesh results in figure 5. Other than the expected differences in smoothness of the fields, the nonlocal stress and slip rate distributions do not appear to be influenced significantly by halving the mesh size.



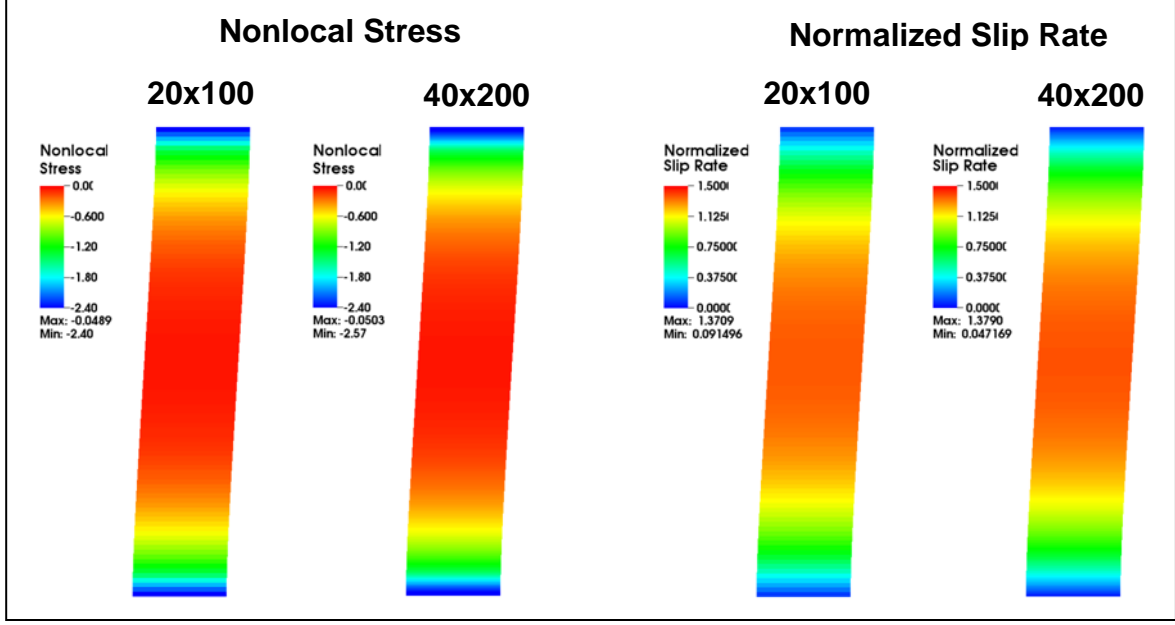


Figure 5. Comparison of nonlocal stress and the slip rate for the  $20 \times 100$  and  $40 \times 200$  element simulations of the 5- $\mu\text{m}$ -thick single crystal. The results are shown at a 0.05 shear strain.

For a more quantitative assessment, the applied shear stress computed at the crystal boundaries is 2.3% lower for the finer mesh. Part of the difference may be due to the lower energy solution expected with an increased number of degrees of freedom, and the remainder can be attributed to discretization error associated with the nonlocal computations and the operator split algorithm. The time step was also a factor of two lower in the fine mesh calculation due to the dependence of the Courant stable time step on the mesh size. The smaller time step improves the accuracy of the operator split integration.

The simulation of the 0.5- $\mu\text{m}$ -thick crystal experienced numerical instabilities when the strain increment per step was too great. This is thought to be associated with the operator split where the strength increase from the slip gradients creates a driving force that is too large and over-corrects the slip rate. Specifically, with a strain increment of  $1.54 \times 10^{-7}$  per time step, the slip rate for the 0.5- $\mu\text{m}$  crystal was erratic and non-zero only in scattered, isolated elements. These isolated regions of slip occurred briefly and died out quickly as deformation proceeds, and eventually strain was incremented in the entire domain, albeit unevenly. When the time step was reduced by a factor of two, such that the strain increment per step was  $7.43 \times 10^{-8}$ , the calculation was well behaved. The results in figures 2 through 4 were run with a strain increment of  $3.853 \times 10^{-8}$  to be certain that the time step was small enough to suppress the instability. The calculations for the larger crystal sizes experienced less gradient hardening, and they were run at the Courant stable time step without any additional time step controls.

### 3.2 Polycrystal Simulations

An idealized polycrystal was created by filling a rectangular region with regular hexagonal grains (figure 6a). Simple shear boundary conditions were applied by prescribing velocities to the nodes on the upper and lower surfaces. Periodic boundary conditions were applied on the left and right surfaces. The orientation of the triangular crystal lattice in each of the grains was random, and the rotation angle from the reference orientation is indicated on the plot. The half grains at the same height on the left and right of the model region were given the same orientation to facilitate application of periodic boundary conditions. As with the single crystal simulations, the initial velocity of all interior nodes was prescribed to eliminate ringing from abrupt imposition of boundary conditions.

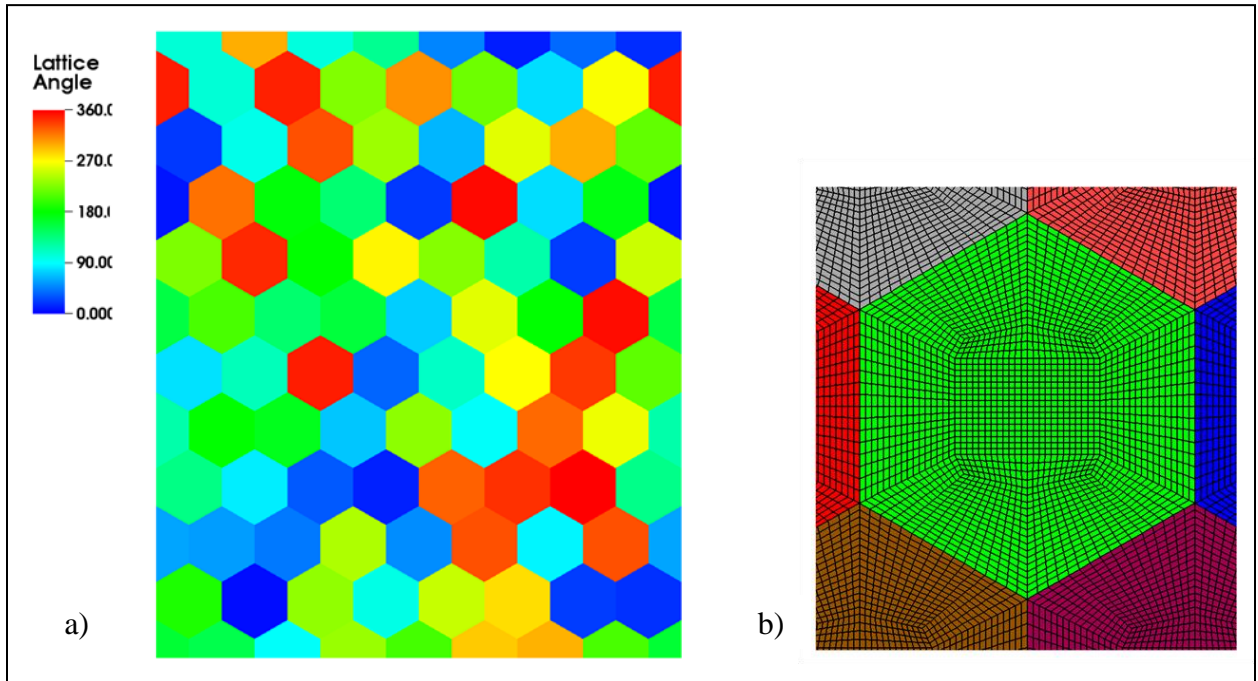


Figure 6. Grain structure (a) and finite element mesh and (b) for the polycrystal simulations.

The default inter-element slip rate condition for all elements is that any element face touching another grain will have restricted slip. This is imposed by assuming that a ghost element across the interface has equal and opposite slip in equation 4. The restricted slip condition is enforced on the upper and lower surfaces and on grain boundaries, including those grain boundaries on the periodic surfaces. The half crystals on the periodic surfaces are treated differently; the element across the interfaces is assumed to have the same slip. This is not a truly periodic condition, but a data structure identifying periodic neighboring elements is not yet available.

Three model sizes are investigated:  $160\sqrt{3} \mu\text{m} \times 300 \mu\text{m}$ ,  $16\sqrt{3} \mu\text{m} \times 30 \mu\text{m}$ , and  $1.6\sqrt{3} \mu\text{m} \times 3 \mu\text{m}$ . All use the same mesh configuration, scaled to give the appropriate dimensions. Each of the 88 hexagons was discretized by an identical mesh of 2112 quadrilateral

elements (figure 6b). Nodes are shared along the grain boundaries, so the deformation is continuous throughout.

Slip rates normalized by the applied shear rate are shown in figure 7 for the three polycrystal sizes. At the larger crystal size the strain rate localizes into well-defined bands. The majority of the deformation is carried by two horizontal bands with some scattered activity in the central region of the model. Blocks of grains appear to remain elastic while localized shear along the horizontal and vertical bands accommodates the deformation between neighboring blocks. The bands do not follow the grain boundaries, but many are associated with grain boundary triple points.

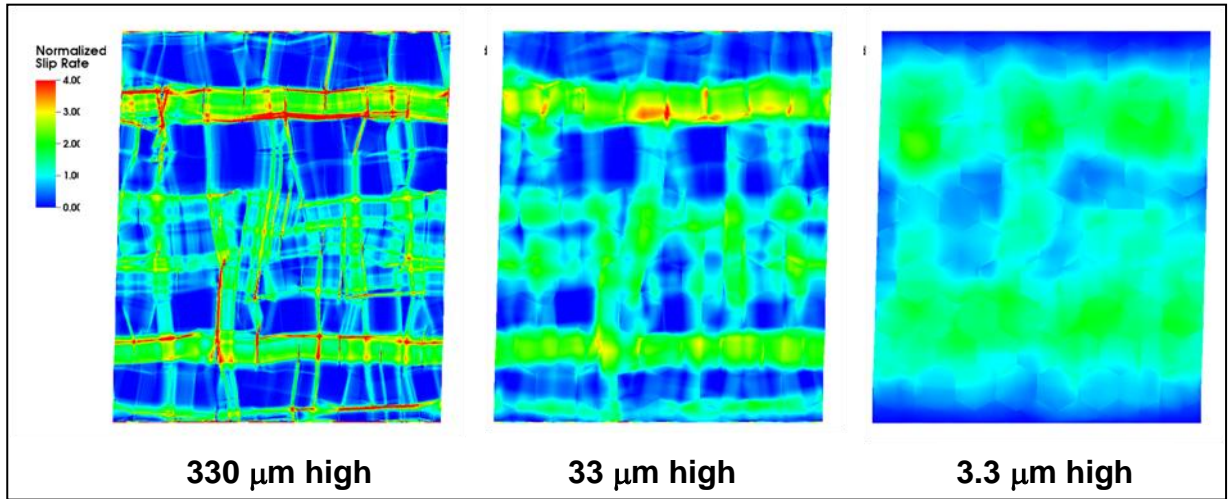


Figure 7. Normalized slip rate distribution for simple shear deformation of idealized polycrystals with heights of 330, 33, and 3.0  $\mu\text{m}$ . The color scale is the same for all three plots.

At the intermediate polycrystal size the nonlocal slip constraint diffuses the deformation. The slip bands are still fairly well defined, but the peak strain rates are not as high and regions of nearly elastic behavior are smaller and less well defined. The slip rates in the 3.3- $\mu\text{m}$ -thick polycrystal are considerably more diffuse and the material near the highly constrained top and bottom boundaries has the lowest strain rates. Grain outlines are evident as the slip rate tends to be high or low at the grain boundaries, and the color contrast across the boundaries accentuates them.

The nonlocal strengthening associated with the gradients is shown in figure 8 for all three slip systems and the three crystal sizes. The color scale in each row is the same so that the magnitude of the effect of the slip systems can be compared. The scales are different for each crystal size as the strengthening is much greater in the smaller model region. The color scale for the 330 mm polycrystal is set to a relatively low value of 0.5 MPa, and even then, the gradient contribution is only evident at the grain boundaries or near the most highly shear regions shown in figure 7. The impact on the solution is minor.

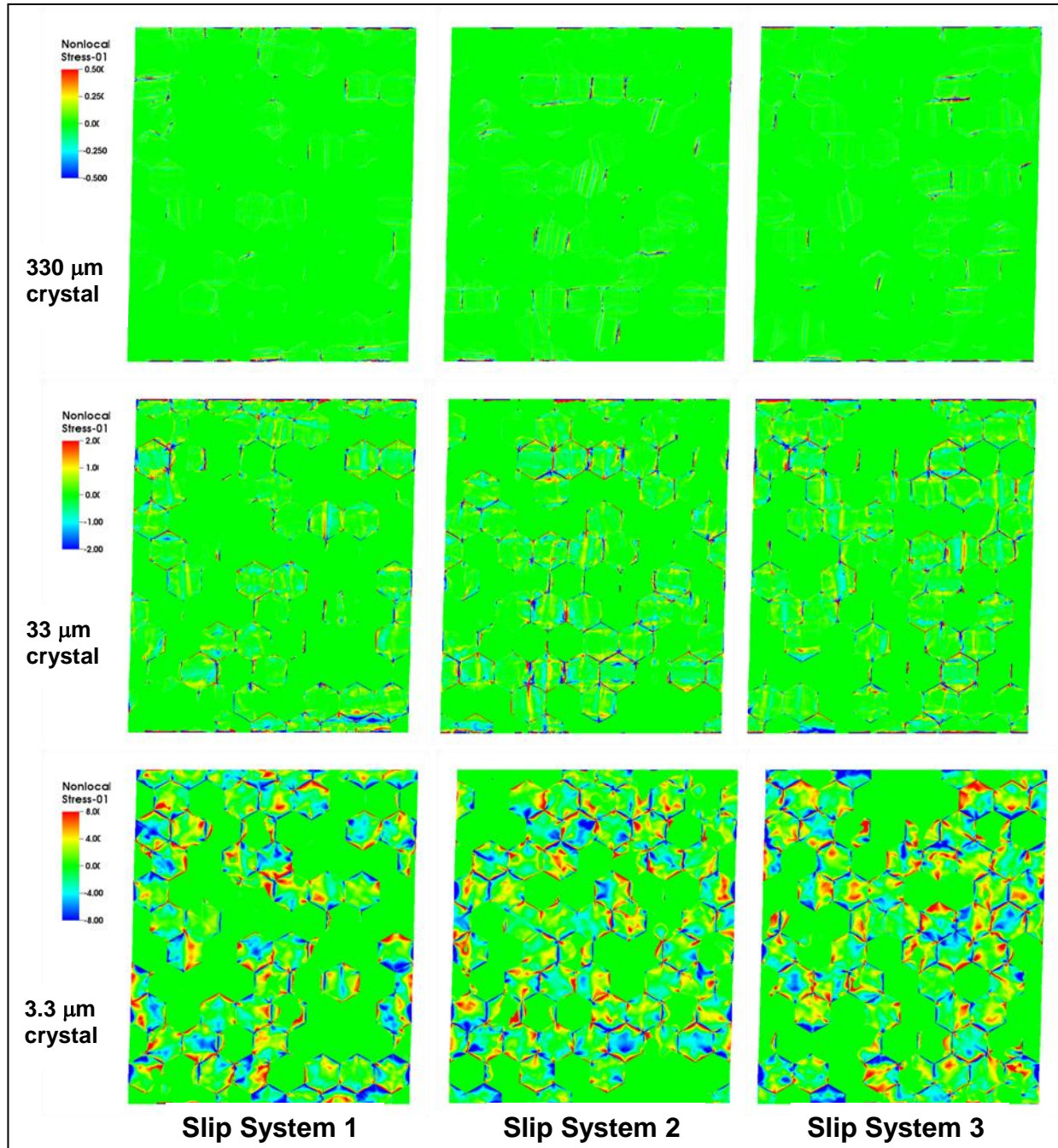


Figure 8. Nonlocal strength contributions on the three slip systems for polycrystal model sizes of 330, 33, and 3.3  $\mu\text{m}$ . The color scales are consistent within each row.

The nonlocal strength distribution in the 33- $\mu\text{m}$  polycrystal appears in the grain interiors as well as at the grain boundaries. The strong interior features are associated with stress concentrations at grain boundary triple points, and most correspond to elevated slip activity in figure 7. Many of the grain boundaries show strengthening on one side and softening on the other. These correspond to increasing slip when approaching grain boundaries for strengthening and decreasing slip when approaching the boundaries for softening.



The nonlocal strengthening is quite prominent in the 3.3- $\mu\text{m}$  polycrystal. As with the intermediate size polycrystal, the sign of the gradient effect is often flipped across the grain boundaries. For most grains, the gradient is strongest at the grain boundaries and decays toward the grain center. However, there are a few notable grains where the peak values are in the interiors. These correspond to locations of intersecting slip activity in figure 7. The hyperbolic tangent function causes the gradient effect to saturate at a level between 12 and 13 MPa. It is also notable that the gradient strengthening occurs on only two of the three slip systems. This reflects the lack of redundant slip for the idealized crystal. Only two slip systems are active at any time.

The shear stress-shear strain response for the three polycrystal sizes is presented in figure 9. As with the single crystals, the stress is higher for the smaller polycrystals. The nonlinearity with length scale is also clearly evident. There are, however, two important distinctions from the single crystal results. The first is that the initial yield point varies with crystal size, whereas it did not for the single crystal simulations. This is thought to be related to the single crystals yielding throughout simultaneously whereas the polycrystal yields gradually and may build up local slip gradients before the macroscopic yield is evident.

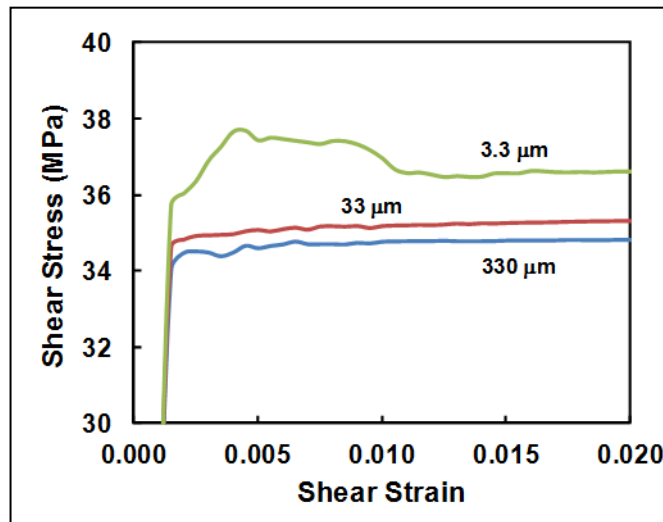


Figure 9. Shear stress strain response for three different size scales of idealized polycrystals.

The other notable difference is that the curves are not smooth. This could result from a combination of the evolution of the crystal lattice orientation, evolution of the slip gradients, and wave propagation in the explicit dynamic calculation. The change in lattice orientation is shown in figure 10 for the largest and smallest size scales. In the 330- $\mu\text{m}$  polycrystal, where the strain localization is more pronounced, lattice reorientation is also localized. The local geometric softening facilitates the shear. In contrast, due to the slip continuity and gradient constraints, the lattice reorientation in the 3.3- $\mu\text{m}$  polycrystal is smoothed over a larger region relative to the grain size, and the lattice within a grain rotates nearly uniformly. A larger portion of the

polycrystal had to realign, which takes longer and results in a greater load excursion before it settles into a nearly steady shear mode.

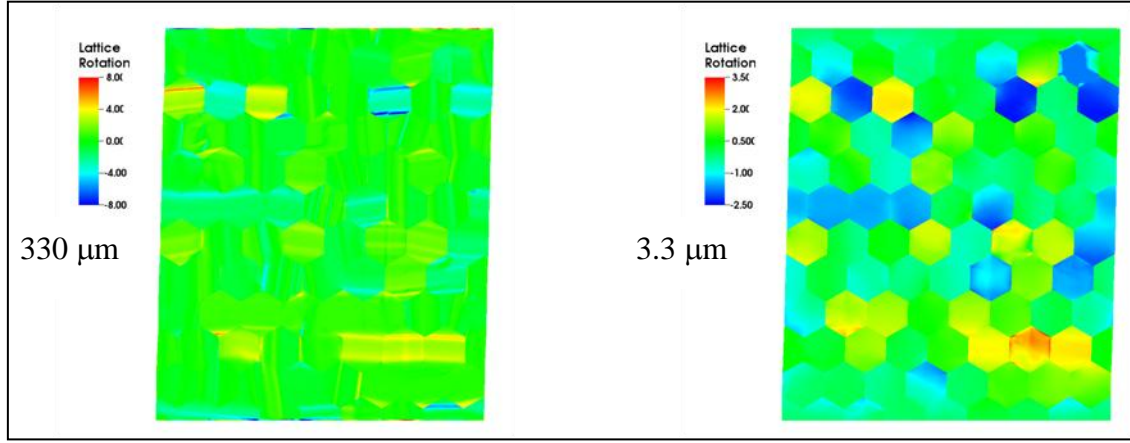


Figure 10. Change in crystal lattice orientation, in degrees, at 0.025 shear strain for the 330- and 3.3-μm-high polycrystals.

#### 4. Physical Size Scale Considerations

The motivation for imposing dislocation flux constraints is that dislocations are discrete entities that propagate from one element to the next as part of the slip process. Another aspect of the dislocation discreteness is their spacing, which is typically quantified in terms of the dislocation density. For well-annealed metals, a typical dislocation density is  $10^6 - 10^7 \text{ cm}^{-2}$ ; at a few percent deformation, this increases to  $10^8 - 10^9 \text{ cm}^{-2}$ , and for a very heavily deformed polycrystal, the dislocation density is in the neighborhood of  $10^{11} \text{ cm}^{-2}$  (7). Table 1 lists the element areas for each of the four single crystal simulations and the higher values of dislocation density for well-annealed, lightly deformed and heavily deformed polycrystalline metals. From these values, an average number of dislocations enclosed by an element is calculated.

Table 1. Average number of dislocations per element expected in the simulations of for well-annealed, lightly deformed and heavily deformed metals.

	<b>50 μm Crystal</b> $E_{\text{length}} = 0.5\mu\text{m}$ $E_{\text{area}} = 0.25\mu\text{m}^2$	<b>5 μm Crystal</b> $E_{\text{length}} = 0.05\mu\text{m}$ $E_{\text{area}} = 0.0025\mu\text{m}^2$	<b>1 μm Crystal</b> $E_{\text{length}} = 0.01\mu\text{m}$ $E_{\text{area}} = 0.0001\mu\text{m}^2$	<b>0.5 μm Crystal</b> $E_{\text{length}} = 0.005\mu\text{m}$ $E_{\text{area}} = 0.000025\mu\text{m}^2$
$10^7 \text{ cm}^{-2} (10^{-1} \mu\text{m}^{-2})$	1/40	1/4000	$10^{-5}$	$2.5 \times 10^{-6}$
$10^9 \text{ cm}^{-2} (10^1 \mu\text{m}^{-2})$	2.5	1/40	1/1000	1/4000
$10^{11} \text{ cm}^{-2} (10^3 \mu\text{m}^{-2})$	250	2.5	1/10	1/40

The entries in table 1 that are less than 1.0 indicate that not every element will contain a dislocation. For example, 1/4000 means that one out of every 4000 elements can be expected to contain a dislocation. An implicit assumption in continuum crystal plasticity models is that the dislocation content in the elements is sufficient for slip to be smooth and continuous. It is clear that these conditions are not met for a well-annealed metal using any of the single crystal meshes since not every element would contain even one dislocation. Using the discretization provided by the 50- $\mu\text{m}$ -thick crystal simulation, a sufficient number of dislocations would be represented within each element when the crystal is heavily deformed, but not in the deformation leading up to that state. Considering that dislocations are usually not uniformly distributed, element sizes of a few microns may be necessary to assure a sufficient number of dislocations per element for a proper continuum crystal model representation.

A further concern is that dislocations are usually less uniformly distributed in heavily deformed metals. They typically organize into walls, which create a cell structure. The cell walls have a very high dislocation density, and the cell interiors have a low dislocation density. Extensive analysis of heavily deformed nickel by Hughes and Hansen (8) shows that these cell sizes are greater than 0.1  $\mu\text{m}$  after cold rolling to a 98% reduction, or a logarithmic strain in excess of 3.9. In order to have a smeared representation of such a cell microstructure within each element, the element size would have to be on the order of 1  $\mu\text{m}$ . If the elements are small enough to resolve the cell structure, there are discrete lattice orientation jumps across the cell walls, not smooth gradients. The crystal plasticity models will have to be enhanced in an alternative manner to include the additional deformation mechanisms.

#### **4.1 Semi-discrete Dislocation Model**

In an attempt to push continuum finite element simulations to smaller length scales where dislocations are sparse within the elements, a semi-discrete model was developed. It is run within a standard explicit-dynamic finite element framework that is described in the first year DRI report (9). The single slip constitutive model follows the traditional formulation with three major modifications: (1) only elements that contain dislocations or dislocation sources can slip; (2) the slip increment is quantized in terms of the Burgers vector and element size; and (3) elements designated to contain dislocation nucleation sources have a reduced flow strength. In addition to these slip model modifications, the code tracks dislocations moving from one element to another, and it also tracks the total number of dislocations that have traversed each element. Details of the model and complete results have been reported elsewhere (1).

Results from a two-dimension, simple shear simulation, 50  $\mu\text{m}$  wide and 100  $\mu\text{m}$  high, are presented in figures 11 and 12. The mesh was  $400 \times 800$  elements, for an element size of 0.125  $\mu\text{m}$ . There were 158 dislocation nucleation sites distributed randomly in the mesh, providing a nucleation site density of approximately  $3.2 \times 10^6 \text{ cm}^{-2}$ . This is in the range of the dislocation density for a well-annealed metal.

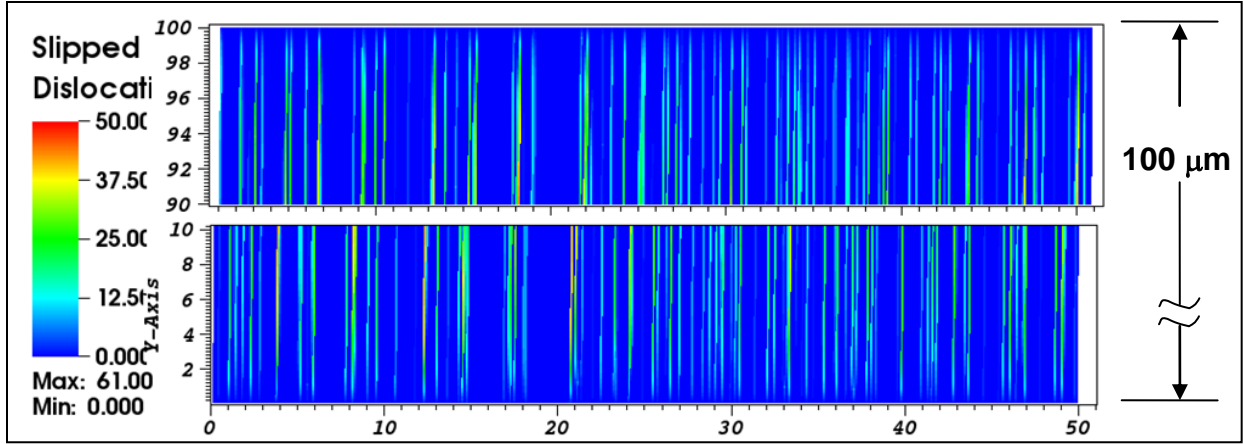


Figure 11. Number of dislocations passing through each element for the discrete dislocation simulations. The center 80  $\mu\text{m}$  is omitted from the 100- $\mu\text{m}$  crystal to highlight the gradients at the top and bottom surfaces.

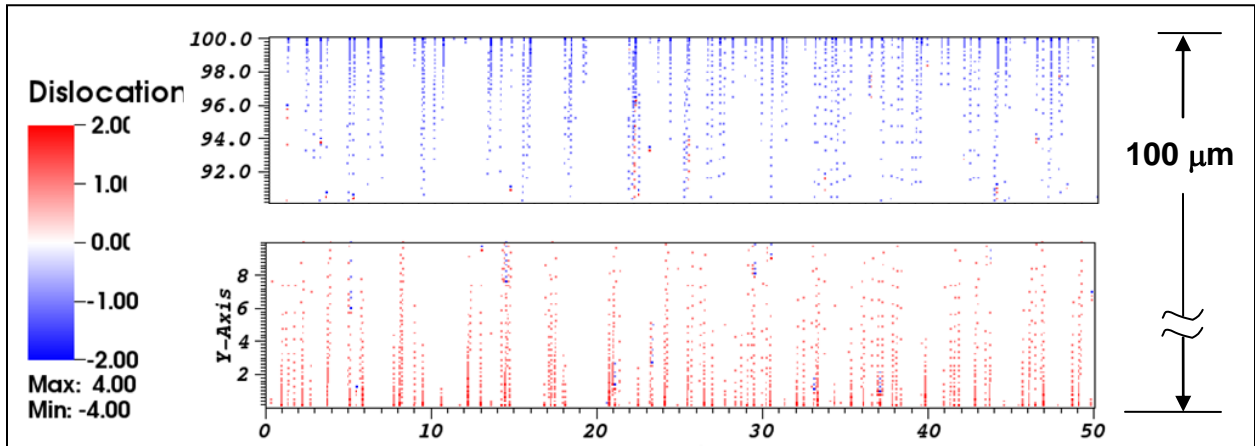


Figure 12. Number of dislocations currently within each element for the discrete dislocation simulations. The center 80  $\mu\text{m}$  is omitted from the 100- $\mu\text{m}$  crystal to highlight the gradients at the top and bottom surfaces.

The number of dislocations that passed through each element at a shear strain of 0.01 is presented in figure 11. Only the top and bottom 10  $\mu\text{m}$  of the 100- $\mu\text{m}$  model are shown since most of the center section appears as lines connecting the upper and lower portions. The most obvious feature is the discrete deformation. Slip occurs only along slip systems containing the nucleation sites. The slip traverses the crystal vertically along lines of elements that contains the slip planes. The remaining elements are elastic. An important feature of figure 11 is the slip gradient. Since dislocations cannot pass through the upper and lower boundaries, the slip (number of dislocations passed) at these surfaces is zero. The greatest number of dislocation has passed near the center of the crystal.

All of the dislocations must lie between the nucleation sites where they originate and the crystal boundaries. The slip distribution is directly related to the current positions of the dislocations. The dislocation positions are shown in figure 12. As with figure 11, only the upper and lower 10  $\mu\text{m}$  are shown for the 100- $\mu\text{m}$ -thick crystal. Dislocations of opposite sign originating at the



dipoles are shown by the red and blue. Dislocations of one sign move to the top and those of the other sign move to the bottom. The dislocation density is greatest at the boundaries and tapers off toward the center of the crystal. This is the classic picture of an edge dislocation pile-up. The dark red and blue elements on the crystal interior indicate the location of the dipole nucleation sites where dislocations can accumulate before gliding toward the boundaries.

Each element can contain multiple dislocations, with the maximum number being four for this simulation. The gradient is evident in the sparseness of elements containing dislocations. Near the surface, most elements along the slip planes contain dislocations, but as the distance from the boundary increases, the elements containing dislocations become increasingly sparse.

While the results of this simple semi-discrete model show dislocation pile-ups and other expected features not captured by standard continuum models, the specific approach is will not produce meaningful results at smaller size scales. The overriding issue is the singular stress field from the dislocations dominating the solution as the mesh is refined to resolve the stress gradients. The stress field is driven by the quantization of slip, which provides a higher stress magnitude related to the better resolution of the singularity at finer spatial resolutions. The unresolved singularity dominates and pollutes the solution. There does not appear to be a range of element sizes that will both resolve the stress field and not suffer from the effects of the singularity. Perhaps other semi-discrete approaches could be successful; this one was not.

Discrete dislocation dynamics simulations (*10, 11*) explicitly account for dislocations and their interactions and provide one means for incorporating dislocation microstructure at finer spatial resolutions. Finite element methods have been coupled with the discrete dislocation simulations though several approaches (*12–14*). These types of formulations should be employed at the finer spatial resolutions in multiscale modeling schemes. There could be a transition from traditional continuum crystal plasticity to proper discrete representation when the spatial resolution is fine enough (*15*).

---

## 5. Conclusions

---

A nonlocal crystal plasticity model, motivated by slip continuity between neighboring finite elements, was implemented in a large-scale parallel finite element code. This is the first large-scale explicit implementation, and the first solution illustrating gradient effects at grain boundaries in a large, dynamic polycrystal simulation. The results show the expected trends of decreasing the severity of gradients and increasing strength with decreasing physical size. In terms of the original objectives, the program was successful.

It is, however, a qualified success. The gradient effects are only significant on the length scale of approximately 100 of  $\mu\text{m}$  or less. It was determined that spatial discretization for such problems can be on the order of, or smaller than, the scale of the underlying microstructure. For lightly

deformed metals, only a small fraction of the elements would contain dislocations, and the continuum crystal plasticity model will not apply. For heavily deformed metals with a dislocation cell structure, the element size can be on the order of the cell structure. The discrete orientation jumps and deformation mechanisms associated with the dislocation cells are not adequately represented by traditional crystal plasticity or the gradient model.

Hence, while the model can be run to obtain results at small size scales, the solutions will not capture the additional physical mechanisms associated with microstructure at the enhanced resolution. The model will not provide significant insight into deformation at the sub-micron scale since the model does not adequately represent the structure or mechanisms at the sub-micron scale.

---

## 6. References

---

1. Becker, R. *Slip Continuity in Explicit Crystal Plasticity Simulations Using Nonlocal Continuum and Semi-discrete Approaches*; ARL-TR-6291; U.S. Army Research Laboratory: Aberdeen Proving Ground, MD, 2013.
2. Bittencourt, E.; Needleman, A.; Gurtin, M. E.; Van der Giessen, E. A Comparison of Nonlocal Continuum and Discrete Dislocation Plasticity Predictions. *J. Mech. Phys. Solids* **2005**, *51*, 281–310.
3. Gurtin, M. E.; Anand, L.; Lele, S. P. Gradient Single-crystal Plasticity with Free Energy Dependent on Dislocation Densities. *J. Mech. Phys. Solids* **2007**, *55*, 1853–1878.
4. ALE3D: An Arbitrary Lagrange-Eulerian 2D and 3D Code System, V-4.16 (2012), A.L. Nichols, ed., Lawrence Livermore National Laboratory.
5. Becker, R. Effects of Crystal Plasticity on Materials Loaded at High Pressures and Strain Rates. *Int. J. Plast.* **2004**, *20*, 1983–2006.
6. Flanagan, D. P.; Belytschko, T. A Uniform Strain Hexahedron and Quadrilateral with Orthogonal Hourglass Control. *Int. J. Num. Meth. Engr.* **1981**, *17*, 679–706.
7. Hull, D.; Bacon, D. J. *Introduction to Dislocations*; 3rd Edition, pg. 22, Pergamon Press, Elmsford, NY.
8. Hughes, D. A.; Hansen, N. Microstructure and Strength of Nickel at Large Strains. *Acta Mater.* **2000**, *48*, 2985–3004.
9. Becker, R. *Dislocation Transport in Continuum Crystal Plasticity Simulations*; ARL-MR-0799; U.S. Army Research Laboratory: Aberdeen Proving Ground, MD, 2011.
10. Kubin, L. P.; Canova, G.; Condat, M.; Devincre, B.; Pontikis, V.; Brechet, Y. Dislocation Microstructures and Plastic Flow: A 3D Simulation, Diffusion and Defect Data-solid State Data B. **1992**, *23–24*, 455–472.
11. Arsenlis, A.; Cai, W.; Tang, M.; Rhee, M.; Oppelstrup, T.; Hommes, G.; Pierce, T. G.; Bulatov, V. V. Enabling Strain Hardening Simulations with Dislocation Dynamics, *Modelling Simul. Mater. Sci. Eng.* **2007**, *15*, 553–595.
12. Van der Giessen, E.; Needleman, A. Discrete Dislocation Plasticity-A Simple Planar Model, *Modelling Simul. Mater. Sci. Eng.* **1995**, *3*, 689–735.
13. Fivel, M. C.; Robertson, C. F.; Canova, G. R.; Boulanger, L. Three-dimensional Modeling of Indent-induced Plastic Zone at a Mesoscale. *Acta Mater.* **1998**, *46*, 6183–6194.

14. Yasin, H.; Zbib, H. M.; Khaleel, M. A. Size and Boundary Effects in Discrete Dislocation Dynamics: Coupling with Continuum Finite Element. *Mater. Sci. Eng. A* **2001**, 309–310, 294–299.
15. Wallin, M.; Curtin, W. A.; Ristinmaa, M.; Needleman, A. Multi-scale Plasticity Modeling: Coupled Discrete Dislocation and Continuum Crystal Plasticity. *J. Mech. Phys. Solids* **2008**, 56, 3167–3180.

---

## **7. Transitions**

---

An ARL Technical Report (ARL-TR-6307) with a more complete description of the models and results is in press. Results of the model limitations were discussed at the Materials in Extreme Dynamic Environments Fall Meeting.

NO. OF COPIES	ORGANIZATION
1 ELEC	ADMNSTR DEFNS TECHL INFO CTR ATTN DTIC OCP 8725 JOHN J KINGMAN RD STE 0944 FT BELVOIR VA 22060-6218
2	US ARMY RSRCH LAB ATTN IMAL HRA MAIL & RECORDS MGMT ATTN RDRL CIO LL TECHL LIB ADELPHI MD 20783-1197
1	US ARMY RESEARCH LAB RDRL-SER-L A E WICKENDEN  <u>ABERDEEN PROVING GROUND MD 21005</u>
1	RDRL-WMP-C R BECKER
1	RDRL-WMP-C T BJERKE